



EPSRC Centre for Doctoral Training
Quantum Engineering



University of
BRISTOL

DOCTORATE OF PHILOSOPHY

Schrödinger's Catwalk

BRIAN FLYNN

UNIVERSITY OF BRISTOL

December, 2020

CONTENTS

I EXPERIMENTAL STUDIES

1	NITROGEN VACANCY CENTRE	2
1.1	nitrogen-vacancy (NV)-centres	2
1.2	Target system	4
1.2.1	Mapping to model terms	5
1.2.2	Experimental procedure	7
1.3	exploration strategy	9
2	EXTENSION TO MANY QUBITS	11
2.1	Genetic algorithm	11

Appendix

A	FIGURE REPRODUCTION	13
B	EXAMPLE EXPLORATION STRATEGY RUN	16

LIST OF TABLES

Table A.1	Figure implementation details	15
-----------	---	----

LIST OF FIGURES

Figure 1.1	nitrogen-vacancy centre energy levels.	3
Figure 1.2	States of spin qubit at each stage of Hahn echo sequence	8
Figure 1.3	Raw data for the nitrogen-vacancy centre's dynamics.	9
Figure 1.4	Quantum Model Learning Agent (QMLA) applied to experimental system.	10

LISTINGS

A.1 "QMLA Launch script"	13
------------------------------------	----

ACRONYMS

AIC	Akaike information criterion. 84, 86
AICC	Akaike information criterion corrected. 84
BF	Bayes factor. 25–27, 33, 35, 48, 51, 55, 57, 61, 63, 64, 80, 81, 87, 89–91, 93–95
BFEER	Bayes factor enhanced Elo ratings. 80, 81, 93, 94, 96
BIC	Bayesian information criterion. 86
CLE	classical likelihood estimation. 13
EDH	experiment design heuristic. 18–23, 26, 35, 45, 55, 56, 83
ES	exploration strategy. 27–31, 33–35, 40, 43, 45, 49, 51, 61, 65, 67, 75, 79, 105, 108
ET	exploration tree. 28, 29, 31, 33–35, 45, 47, 75
FH	Fermi-Hubbard. 58
FP	false negatives. 78
FP	false positives. 78
GA	genetic algorithm. iii, 34, 67, 71, 74, 75, 80, 82, 83, 88, 90, 93, 96–98
GES	genetic exploration strategy. 67, 78, 93, 94, 97
HPD	high particle density. 18
IQLE	interactive quantum likelihood estimation. 13, 14, 93, 94
LTL	log total likelihood. 16
ML	machine learning. 6, 26, 27, 78
MS	model search. 27–29, 31, 35, 43, 45
MVEE	minimum volume enclosing ellipsoid. 18

NV	nitrogen-vacancy. 9
NVC	nitrogen-vacancy centre. 14
OF	objective function. iii, 67, 68, 74, 75, 78, 80, 81, 83, 84, 88, 91–93
PGH	particle guess heuristic. 19, 20, 45
QHL	quantum Hamiltonian learning. 8–14, 16, 18, 20–22, 25–27, 31–35, 40, 43, 48, 55, 56, 75, 93, 94, 105
QL	quadratic loss. 17
QLE	quantum likelihood estimation. 13, 32
QMLA	Quantum Model Learning Agent. ii, iii, vii, 8, 13, 24, 25, 27–31, 34, 35, 40, 43–49, 51, 52, 60, 61, 63–65, 67, 72, 74–77, 83, 87, 88, 90, 91, 93, 94, 96–98, 105
SMC	sequential monte carlo. 11–13, 15, 18, 19, 22, 31
TLTL	total log total likelihood. 16, 25–27, 35, 84, 91
TN	true negatives. 78
TP	true positives. 78

GLOSSARY

Jordan Wigner transformation (JWT)	Jordan Wigner transformation . 60, 61, 64
Loschmidt echo (LE)	Quantum chaotic effect described. . 14
chromosome	A single candidate in the space of valid solutions to the posed problem in a genetic algorithm. . 68
gene	Individual element within a chromosome. . 68
hyperparameter	Variable within an algorithm that determines how the algorithm itself proceeds.. 11
instance	a single implementation of the QMLA algorithm. iii, 48, 94, 97, 98, 105
likelihood	Value that represents how likely a hypothesis is.. 10, 13, 15, 18, 31, 33, 34, 36, 88
model	The mathematical description of some quantum system. 24
model space	Abstract space containing all descriptions (within defined constraints such as dimension) of the system as models. 29
probe	Input probe state, $ \psi\rangle$, which the target system is initialised to, before unitary evolution. plural. 13, 15, 18–22, 54
results directory	Directory to which the data and analysis for a given run of QMLA are stored. . 49
run	collection of QMLA instances. iii, vii, 48, 49, 64, 65, 94, 96, 98, 105
spawn	Process by which new models are generated by combining previously considered models.. 29
success rate	. 48, 49

term	Individual constituent of a model, e.g. a single operator within a sum of operators, which in total describe a Hamiltonian. . 24
volume	Volume of a parameter distribution's credible region.. 18, 55, 56, 63
win rate	. 48, 49

Part I

EXPERIMENTAL STUDIES

It is of primary interest to apply the QMLA algorithm to real-life, experimental systems. In this chapter we devise an exploration strategy (ES) to operate in conjunction with experimental data in order to characterise an electron spin in an NV centre in diamond. In particular, we model, through Hamiltonian terms, interactions between the spin and the spin bath in which it resides, so that QMLA is finding an effective model for the open system dynamics.

Here we will first introduce a basic picture of nitrogen-vacancy centres (NVCs), using basic but nonstandard nomenclature for simplicity; for thorough descriptions of the underlying physics, readers are referred to [1]. We next discuss the target system with respect to its modelling, determining the suitable terms which *might* represent the NVC's interactions, to inform the starting point for the QMLA. Finally we describe the implementation of an ES for the examination of the NVC, and the results of the QMLA procedure.

1.1 NV-CENTRES

NV centers are point defects in diamond, occurring naturally [2] or synthetically [3, 4]. A substitutional nitrogen-14 (^{14}N) isotope is embedded in a lattice of carbon atoms in diamond, adjacent to a lattice vacancy, such that it is surrounded by three carbon-13s (^{13}Cs) [5]. Of the ^{14}N atom's five valence electrons, three bond with nearby ^{13}Cs ; the remaining two unbonded electrons form a lone pair and can be thought of as a single spin- $\frac{1}{2}$ particle. The adjacent lattice vacancy has three unbonded electrons, two of which bond together leaving a single unpaired electron. The single electron in the lattice vacancy, together with the effective lone pair of the ^{14}N , form a system of two spin- $\frac{1}{2}$ particles. Such systems have been thoroughly studied; of particular interest are the resultant *triplet* states, i.e. the allowed permutations of the two particles with total quantum spin $S = 1$, with magnetic spin multiplicity allowing $m_s = -1, 0, 1$, giving rise to three distinct energy levels for the system.

A *manifold* is a set of states differing only slightly, for example states near the absolute ground state manifold might differ only in magnetic spin quantum number, and can be characterised as the ground state manifold. We consider two principle manifolds of the system: the ground state and excited manifolds, each consisting of three states, corresponding to the allowed values for magnetic spin m_s , see Fig. 1.1a. For brevity, we denote states with reference to their magnetic spin and manifold, e.g. the state in the ground state manifold with $m_s = 0$ is denoted $|m_s = 0\rangle_g$. In the absence of a magnetic field, the states corresponding to $|m_s = \pm 1\rangle$ are degenerate, but in the presence of a magnetic field, B , they have distinct energy levels, referred to as the Zeeman effect, Fig. 1.1b.

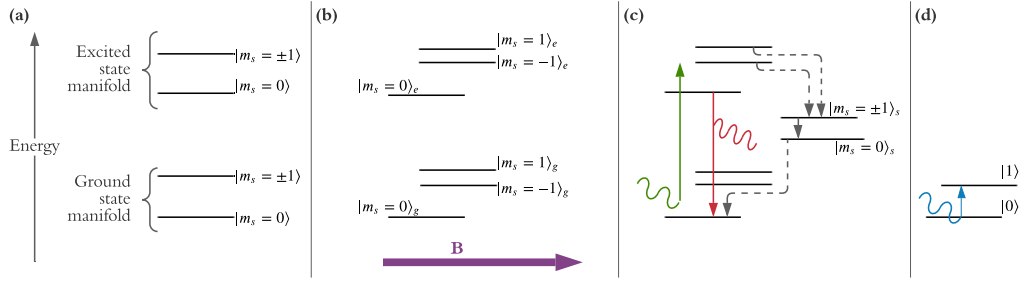


Figure 1.1: Simplified depiction of energy levels of the nitrogen-vacancy centre, corresponding to its triplet state. **a**, With no external field, the system simply has excited and ground-state manifolds, each of which consist of two energy levels depending on the magnetic spin, m_s . **b**, In the presence of a magnetic field (purple, B), the magnetic spins have distinct energy levels, i.e. Zeeman splitting. States are denoted by their magnetic spin and subscripted by their manifold. **c**, Application of a green (532nm) laser excites the NVC from any of the states in the ground state manifold to the excited manifold. The dominant decay mechanism for the excited states are shown: (i) $|m_s = 0\rangle_e \rightarrow |m_s = 0\rangle_g$ (red line) through the emission of a red (637nm) photon; (ii) $|m_s = \pm 1\rangle_e \rightarrow |m_s = 0\rangle_g$ (dotted grey lines) via the shelving manifold which allows for non-spin-preserving transition, and does not emit a photon. **d**, Computational basis states $|0\rangle$ and $|1\rangle$ are assigned to the two lowest energy states. The difference in energy between these states is such that a microwave (MW, blue) photon can trigger transition from $|0\rangle$ to $|1\rangle$, as well as states in between such as $|+\rangle$, allowing for the implementation of quantum logic gates.

We designate the state $|m_s = 0\rangle_g$ as the basis state $|0\rangle = \begin{pmatrix} 1 \\ 0 \end{pmatrix}$, and $|m_s = -1\rangle_g$ as $|1\rangle = \begin{pmatrix} 0 \\ 1 \end{pmatrix}$, such that we have defined a qubit and computational basis, Fig. 1.1d. By shining a laser of 532nm (green) on the NVC, it is excited to the excited manifold, from which it decays back to the ground state manifold. Importantly, the process of this decay can be exploited for the preparation of the NVC in the computational basis state $|0\rangle$. That is, the dominant decay process from $|m_s = 0\rangle_e$ is spin-preserving, so it ends in $|m_s = 0\rangle_g$. On the other hand, had the NVC been in the $|m_s = \pm 1\rangle_e$, the dominant decay process is through a shelving (singlet) state, and does not preserve spin, such that it also decays to the $|m_s = 0\rangle_g$. Therefore, irrespective of the initial state, by shining the green laser on the NVC, it is most likely that it has been prepared in $|m_s = 0\rangle_g = |0\rangle$, providing us a starting point from which to perform computation.

The difference in energy between $|0\rangle$ and $|1\rangle$ is addressible optically: by shining a pulse at the NVC, we can oscillate the qubit between the two levels. Likewise, having initialised the state to $|0\rangle$, we can perform a $\pi/2$ rotation about the logical z-axis, by running the laser for half the time, resulting in the state $|+\rangle$. We can similarly devise radiation to achieve quantum gates and operations on our NVC qubit. We depict these cycles in Fig. 1.1c.

We can further exploit the decay mechanism to compose a readout procedure, to infer the population of $\{|0\rangle, |1\rangle\}$ at a given instant, for example following the application of gates to the system. We know that the excitation due to the green laser is spin-preserving, i.e. when the NVC has been excited to $|m_s = 0\rangle_e$, it had originated in $|m_s = 0\rangle_g$. We also know that the decay $|m_s = 0\rangle_e \rightarrow |m_s = 0\rangle_g$ is spin preserving, with the emission of a red photon: by simply counting the number of photons emitted, we quantify the population of $|0\rangle$ at the time of query. On the contrary, when the $|m_s = -1\rangle_g$ is excited, spin is also preserved, so it goes to $|m_s = -1\rangle_e$; but $|m_s = -1\rangle_e$ decays through the shelving state as outlined earlier, *without* the emission of a photon. We can hence infer the population of $|m_s = -1\rangle_g$ at the time of query by the fraction of incidents which don't emit a photon. That is, say we first calibrate the system by retaining the green laser for some time: after a few μs , a steady state is achieved where the majority of the time, the triplet is in the state $|0\rangle = |m_s = 0\rangle_g$. Then, excitation from the same laser results in the excitation to $|m_s = 0\rangle_e$, which decays back to $|m_s = 0\rangle_g$ and emits a photon in the process; by counting the red photons emitted in a certain time window – equivalently, measuring the photoluminescence (PL) signal – we benchmark the population of $|0\rangle$ when nothing else has happened as p_0 . Now, when we apply gates (i.e. pulses) to the NVC, we can similarly read out the population of $|0\rangle$ as p'_0 , and infer that the likelihood that the is found in the initial state $|0\rangle$ is p'_0/p_0 . We can use this quantity as the likelihood within quantum likelihood estimation (QLE), allowing us to learn from the NVC, as we will discuss in the next sections.

In summary then, by assigning basis states $|0\rangle, |1\rangle$ to energy levels of the ground state manifold, we are able to ensure the preparation of the NVC in $|0\rangle$ by first shining a green laser on the NVC. We can then apply radiation to achieve quantum logical gates on the system, and read out the final state of the system, again by shining a green laser and observing the emitted photons (PL) and inferring the population level of each basis state. We represent these concepts in a simplified format in Fig. 1.1.

1.2 TARGET SYSTEM

We take the axis of the NVC, i.e. the axis connecting the ^{14}N with the lattice vacancy, as the z-axis. There are clearly a huge number of interactions to which the NVC is subject: we choose to focus on its interactions with the environment, i.e. with nuclei in the same diamond, which dictate its decoherence. These interactions are characterised by hyperfine terms [6]. The overall Hamiltonian for such systems, where the set of nuclear sites is $\{\chi\}$, is given by

$$\hat{H}_{\text{full}} = \Delta_{\text{gs}} \hat{S}_z^2 + \mu_B g \mathbf{B} \cdot \mathbf{S} + \mathbf{S} \cdot \sum_{\chi} (\mathbf{A}_{\chi} \cdot \hat{\mathbf{I}}_{\chi}) + P \hat{I}_z^2 + \mu_n g \mathbf{B} \cdot \sum_{\chi} \hat{\mathbf{I}}_{\chi}. \quad (1.1)$$

We will describe each term, as well as approximations which enable us to simplify the space considerably.

- Isolated-spin terms, i.e. describing the spin independent of the environmental nuclei

- $\Delta_{gs}\hat{S}_z^2$: the *zero-field* splitting, i.e. without any external (magnetic) field, the spin oscillates rapidly, with $\Delta_{gs} \sim \text{GHz}$.
- $\mu_B g \mathbf{B} \cdot \mathbf{S}$: the spin's precession about the magnetic field, $\mathbf{B} = (B_x \ B_y \ B_z)$, via the total spin operator¹ $\mathbf{S} = (\hat{S}_x \ \hat{S}_y \ \hat{S}_z)$, where μ_B is the Bohr magneton and g is the g -factor (≈ 2 , simplified from the g -factor tensor).
- Hyperfine terms
 - $\hat{S} \cdot \sum_{\chi} (\mathbf{A}_{\chi} \cdot \hat{I}_{\chi})$: The NVC total spin operator \mathbf{S} couples with each site, χ . At each site there is a nucleus which has total spin operator $\mathbf{I}_{\chi} = (\hat{I}_x \ \hat{I}_y \ \hat{I}_z)_{\chi}$. \mathbf{A} is the hyperfine tensor, containing the hyperfine parameters of interest.
- Bath-only terms, i.e. describing the other nuclei independent of the spin
 - $P\hat{I}_z^2$: the quadrupole splitting, i.e. this term gives the splitting of the ^{14}N 's hyperfine splitting, which does not meaningfully contribute to the short-decay processes in the experiments described in the next section.
 - $\mu_n g \mathbf{B} \cdot \sum_{\chi} \hat{I}_{\chi}$: μ_n is the nuclear magneton and g is again the g -factor.

Given that we are interested in the spin and its interactions with the environment only, we can immediately drop the bath-only terms, by assuming the bath is static apart from its interactions with the NVC. This is a usual assumption in the treatment of open system dynamics, to allow for focus on the dominant interactions for the system of interest [7]. Additionally, since the zero field splitting contributes a constant shift in energy, we can safely omit it by moving to the rotating frame. We are then left only with the second and third terms of ??.

1.2.1 Mapping to model terms

Next we will focus on mapping the remaining terms to operators to compose the set of terms \mathcal{T} to use in our ES. In our modelling, the NVC spin is represented by the first logical qubit, with a further $|\{\chi\}|$ qubits, each representing a unique nuclear site, as discussed later in this section. As standard, we take the axis² of the NVC as parallel to the qubit's z -axis.

The first terms included come from the spin's precession about the magnetic field. It is usually assumed that the external, applied magnetic field is well-aligned with the spin qubit's z -axis; here we will treat this determination as the role of QMLA, i.e. we will endeavour to establish whether the x -, y -axis components of the magnetic field are important for describing the spin's dynamics. Then, we have

$$\mu_B g \mathbf{B} \cdot \mathbf{S} = \mu_B g (B_x \ B_y \ B_z) \cdot (\hat{S}_x \ \hat{S}_y \ \hat{S}_z) \rightarrow \alpha_x \hat{S}_x + \alpha_y \hat{S}_y + \alpha_z \hat{S}_z, \quad (1.2)$$

¹ We invoke an inexact representation of high dimensional tensors here for ease of interpretation. For instance, the total nuclear spin operator exists in arbitrary dimension (depending on the number of sites modelled), but we present it simply as $\mathbf{I} = (\hat{I}_x \ \hat{I}_y \ \hat{I}_z)$ at each site to convey that we can separate the terms in the construction of models.

² The axis connecting the ^{14}N with the lattice vacancy.

with $\alpha_i = \mu_B g B_i$. The spin's rotation terms to be included in QMLA's deliberations are therefore

$$\mathcal{T}_s = \{\hat{S}_x, \hat{S}_y, \hat{S}_z\} \quad (1.3)$$

Next, let's focus on the hyperfine coupling term. In general we sum over the nuclear sites $\{\hat{H}_i\}$, since the spin will interact with every nucleus to some extent; We show in [8] that a realistic system requires modelling a finite-size bath of $|\{\chi\}| \sim 15$ nuclei to capture the dynamics of interest, which is infeasible for complete characterisation via classical simulation, where we are limited to ~ 11 qubit calculations³. Instead, by focusing only on the *short-time* dynamics of the NVC, we can isolate the effects of dominant interactions, most notably with a single nearby ^{13}C . Indeed, by assigning a first qubit as representing the NVC spin, we can map the entire environment onto a generic second *environmental qubit*, representing the amalgamation of said interactions, though we can think of the two-qubit system as the NVC coupled with a single ^{13}C [6].

$$\mathbf{S} \cdot \sum_{\chi} (\mathbf{A}_{\chi} \cdot \mathbf{I}_{\chi}) \rightarrow \mathbf{S} \cdot \mathbf{A} \cdot \mathbf{I} \quad (1.4)$$

This clearly reduces the dimension of our approximation, the number of qubits, n_q from $n_q = 1 + |\{\chi\}|$ to $n_q = 2$, since now we only retain qubits for the NVC and the ^{14}N (which also represents the entire bath). The hyperfine tensor \mathbf{A} consists of the hyperfine parameters, i.e. the strength of corresponding interactions.

$$\mathbf{A} = \begin{pmatrix} A_{\perp} & 0 & 0 \\ 0 & A_{\perp} & 0 \\ 0 & 0 & A_{\parallel} \end{pmatrix}, \quad (1.5)$$

where A_{\perp} is the non-axial hyperfine coupling term and A_{\parallel} is the axial coupling term, since the axis of the NVC is used to define the z-axis for our qubits.

The total spin operators – of the NVC operating on the first logical qubit and the environmental qubit on the second – can be thought of as

$$\begin{aligned} \mathbf{S} &= (\hat{S}_x^{(1)} \quad \hat{S}_y^{(1)} \quad \hat{S}_z^{(1)}) \\ \mathbf{I} &= (\hat{I}_x^{(2)} \quad \hat{I}_y^{(2)} \quad \hat{I}_z^{(2)}) \end{aligned} \quad (1.6)$$

So we can write,

$$\begin{aligned} \mathbf{S} \cdot \mathbf{A} \cdot \mathbf{I} &= A_{\perp} \hat{S}_x \hat{I}_x + A_{\perp} \hat{S}_y \hat{I}_y + A_{\parallel} \hat{S}_y \hat{I}_y \\ &\quad + A_{xy} (\hat{S}_x \hat{I}_y + \hat{S}_y \hat{I}_x) \\ &\quad + A_{xz} (\hat{S}_x \hat{I}_z + \hat{S}_z \hat{I}_x) \\ &\quad + A_{yz} (\hat{S}_y \hat{I}_z + \hat{S}_z \hat{I}_y) \end{aligned} \quad (1.7)$$

Off-diagonal terms, referred to hereafter as *transverse* terms ($\hat{S}_i \hat{I}_j$ where $i \neq j$), are usually neglected [9]; here we will employ QMLA to determine whether their contributions are worthy of inclusion, although we consider only $\{\hat{S}_x \hat{I}_y, \hat{S}_x \hat{I}_z, \hat{S}_y \hat{I}_z\}$ for brevity. In total then, the hyperfine terms to be entertained by QMLA are

$$\mathcal{T}_{HF} = \begin{Bmatrix} \hat{S}_x \hat{I}_x, & \hat{S}_y \hat{I}_y, \hat{S}_z \hat{I}_z, \\ \hat{S}_x \hat{I}_y, & \hat{S}_x \hat{I}_z, \hat{S}_y \hat{I}_z \end{Bmatrix}. \quad (1.8)$$

Finally, combining Eq. (1.3) and Eq. (1.8), we have the full set of terms to incorporate into QMLA ES:

$$\mathcal{T}_{NV} = \begin{Bmatrix} \hat{S}_x, & \hat{S}_y, \hat{S}_z, \\ \hat{S}_x \hat{I}_x, & \hat{S}_y \hat{I}_y, \hat{S}_z \hat{I}_z, \\ \hat{S}_x \hat{I}_y, & \hat{S}_x \hat{I}_z, \hat{S}_y \hat{I}_z \end{Bmatrix}. \quad (1.9)$$

We introduce a shorthand notation to ease model representation for the remainder of this chapter. Recall that we have defined a two-qubit Hilbert space for model construction. Terms which affect only the spin only act on the first qubit, $\hat{S}_i = \hat{\sigma}_i \otimes \hat{\mathbb{1}}$, where $\hat{\sigma}_i$ is the Pauli operator giving rotation about the i -axis, and $\hat{\mathbb{1}}$ is the one-qubit identity matrix. Retaining the hyperfine notation, for the expectedly-dominant diagonal terms, we denote $\hat{A}_i = \hat{S}_i \hat{I}_i = \hat{\sigma}_i \otimes \hat{\sigma}_i$. We refer to the less-dominant off-diagonal terms as *transverse* terms, $\hat{T}_{kl} = \hat{S}_k \hat{I}_l = \hat{\sigma}_k \otimes \hat{\sigma}_l$. We can hence rewrite Eq. (1.9) as

$$\mathcal{T}_{NV} = \begin{Bmatrix} \hat{S}_x, & \hat{S}_y, \hat{S}_z, \\ \hat{A}_x, & \hat{A}_y, \hat{A}_z, \\ \hat{T}_{xy}, & \hat{T}_{xz}, \hat{T}_{yz} \end{Bmatrix}. \quad (1.10)$$

1.2.2 Experimental procedure

We have decided to characterise the hyperfine interactions of the NVC; these are evident most strongly at very short timescales [10]. To isolate the effects of the hyperfine interactions, we run Hahn echo experiments, which are known to emphasise weak interactions. Hahn echo sequences attempt to decouple the spin's dynamics from the nuclear bath [?, 9, 10, 11, 12] providing a helpful platform for studying residual contributions of terms in Eq. (1.10). The NVC qubit undergoes a series of evolutions – either according to application of quantum logic gates or the natural evolution of the system interacting with its environment. We depict the stages of the experiment in Fig. 1.2, starting from the initialised $|0\rangle$ through to its final state which is read out through PL, both of which as described in Section 1.1.

³ This limitation arises from the requirement to compute the total evolution of the global state, involving calculation of $e^{-i\hat{H}t}$, i.e. the characterisation of an n_q -qubit model depends on classical exponentiation of the $2n_q \times 2n_q$ Hamiltonian for each particle and experiment in classical likelihood estimation (CLE), which is a prohibitive expense.

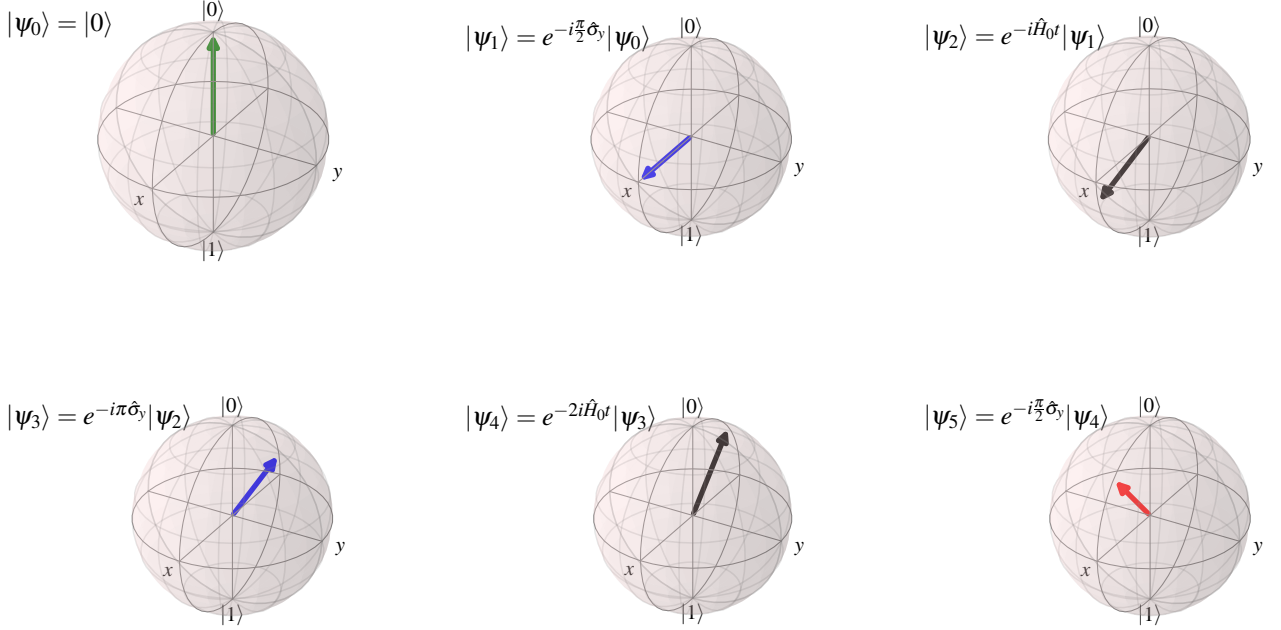


Figure 1.2: States of spin qubit at each stage of Hahn echo sequence.

The state of the NVC spin is initialised by a green laser into state $|\psi_0\rangle = |0\rangle$. We then apply a rotation about the y -axis (i.e. a pulse), yielding the state $|\psi_1\rangle = |+\rangle$. The system is then allowed to evolve according to its own \hat{H}_0 for t , $|\psi_2\rangle = e^{-i\hat{H}_0 t} |+\rangle$. We apply a second pulse, this time for a π -rotation about the y -axis, $|\psi_3\rangle = e^{-i\pi\hat{\sigma}_y} e^{-i\hat{H}_0 t} |+\rangle$. Again the system evolves according to interactions with the environment, this time for $2t$. We apply a final pulse to rotate about the y -axis again, effectively either returning the spin to near the $|0\rangle$ axis, or near the $|1\rangle$ axis. Here $|\psi_5\rangle$ is roughly half way between $|0\rangle$ and $|1\rangle$, i.e. along the z -axis. The spin is read out from $|\psi_5\rangle$ via the NVC's photoluminescence. Here $\hat{H}_0 = 0.25 \hat{\sigma}_y$ was evolved for $t = 0.5$ (arbitrary units), and the final state overlap with the initial state, i.e. the likelihood of measuring the spin in $|0\rangle$ is $\Pr(0|\hat{H}_0, t) = 0.865$.

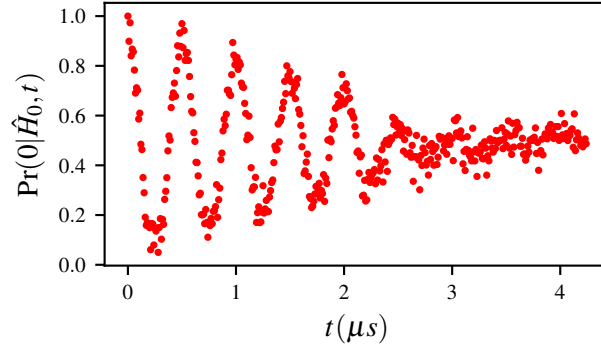


Figure 1.3: Raw data for the nitrogen-vacancy centre's dynamics. The y -axis shows the photoluminescence of the NVC, equivalently the likelihood $\Pr(0|\hat{H}_0, t)$.

In particular, the final state, $|\psi\rangle_5$, is read out, effectively by projection onto $|0\rangle$; we can interpret the PL after evolution time t as the likelihood that the NVC is found in $|0\rangle$ after evolution of its *true* Hamiltonian, \hat{H}_0 . That is, we assign this projection as the quantity $\Pr(0|\hat{H}_0, t)$ (the likelihood), and it can be used within likelihood estimation in order to refine a candidate model \hat{H}_j , effectively⁴ by changing the structure of \hat{H}_j until $\Pr(0|\hat{H}_0, t) \approx \Pr(0|\hat{H}_j, t) \forall t$.

By varying the evolution time of the Hahn-echo sequence, we can map the likelihood against time, which we can view as capturing the dynamics of the NVC spin $??$. We vary time up to $t \approx 4\mu s$ in the short-time-range in intervals of $\Delta t = 50ns$, so we have 425 data points. Importantly, the data for the studied NVC is taken once and analysed offline, i.e. QMLA does not have complete authority to design experiments to run on the NVC, although it can aim to choose the most informative t available in the predefined set; we will discuss the consequences of this restriction later in this chapter.

1.3 EXPLORATION STRATEGY

Finally, then, we are in a position to marry the concepts of

⁴ Of course this is a gross simplification of quantum Hamiltonian learning (QHL) which is described fully in ??

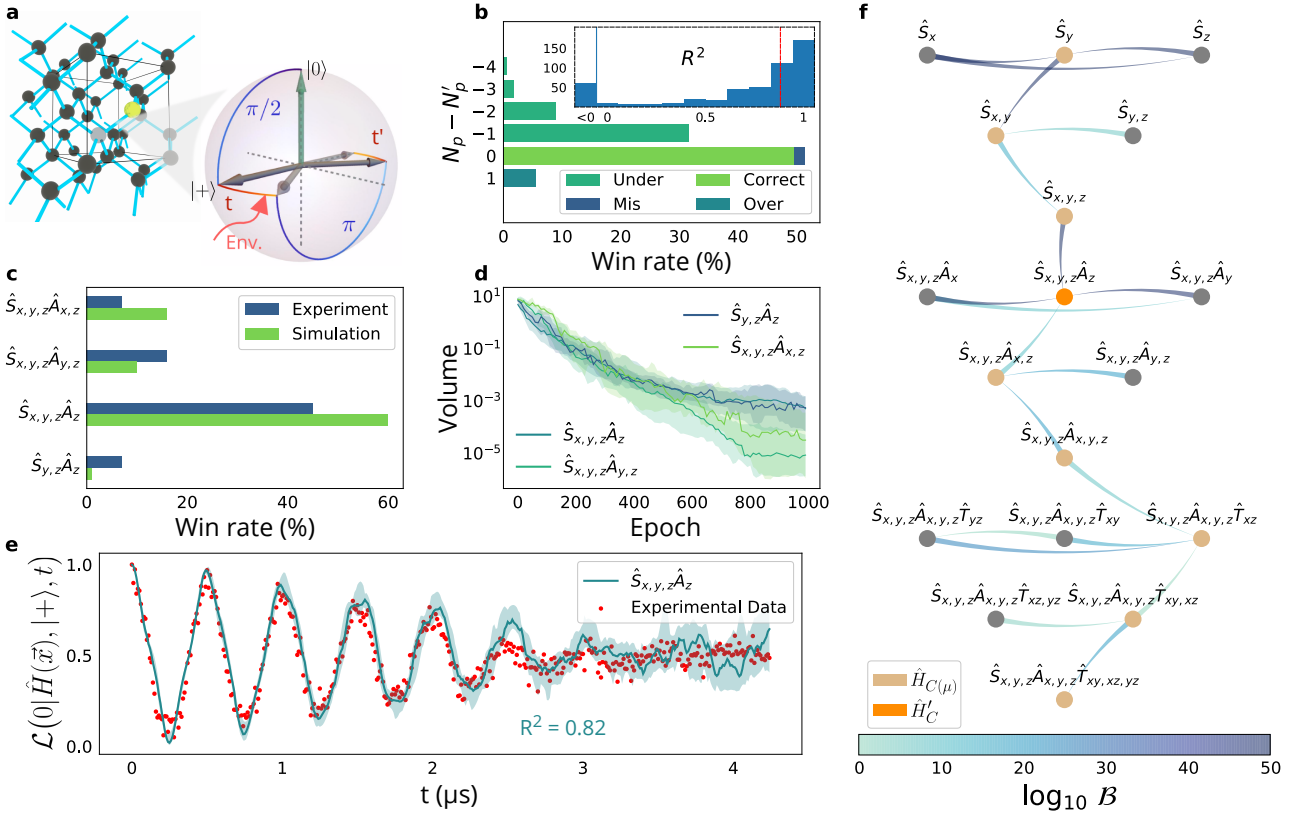


Figure 1.4: **a**, The carbon lattice providing the outer environment for the NV centre, along with the time evolution of the electron spin state (represented on a Bloch sphere) during the pulses for the Hahn-echo sequences. The final $\pi/2$ pulse is omitted. **b**, Simulation of 500 independent QMLA instances, where \hat{H}_0 is chosen randomly. The win rate is reported against the difference ($N_p - N'_p$) between the number of parameters in the QMLA-selected (\hat{H}') and true models, respectively. The *under-parameterised* (*over-parameterised*) class refers to models with less (more) parameters than \hat{H}_0 . *Correct* indicates that exactly \hat{H}_0 was found. The *mis-parameterised* class groups models with the same parametrisation cardinality as \hat{H}_0 , but different Hamiltonian terms. **Inset**, Histogram of occurrences of R^2 values for each retrieved \hat{H}' against a sampling of datapoints from \hat{H}_0 , with median $R^2 = 0.84$ (red dotted line). **c**, Win rates of top four models (see main text), for 100 QMLA instances, against both simulated and experimental data. Simulations use $\hat{H}_0 = \hat{S}_{xyz}\hat{A}_z$. **d**, Total volume spanned by the parameters' prior across epochs, for the models in c. Shaded areas indicate 66% credible regions. **e**, Simulated likelihoods reproduced by the model with the highest win rate ($\hat{S}_{x,y,z}\hat{A}_z$, turquoise), compared with corresponding NV-centre system experimental data (red-dots, extracted from the observed PL of the first microseconds in Hahn-echo decay). Error bars smaller than the dots (see Methods). **f**, A single QMLA instance against experimental data in e, depicted as a , see Fig. ??c. The thin end of each edge points to the favoured model; the colour of the edges maps $\log_{10} \mathcal{B}$ as in the bar legend at the bottom. Layer champions are in light brown, whereas the global champion \hat{H}' is in orange.

EXTENSION TO MANY QUBITS

2.1 GENETIC ALGORITHM

APPENDIX

FIGURE REPRODUCTION

Most of the figures presented in the main text are generated directly by the QMLA framework. Here we list the implementation details of each figure so they may be reproduced by ensuring the configuration in Table A.1 are set in the launch script. The default behaviour of QMLA is to generate a results folder uniquely identified by the date and time the run was launched, e.g. results can be found at the *results directory* `qmla/Launch/Jan_01/12_34`. Given the large number of plots available, ranging from high-level run perspective down to the training of individual models, we introduce a `plot_level` $\in \{1, \dots, 6\}$ for each run of QMLA: higher `plot_level` informs QMLA to generate more plots.

Within the results directory, the outcome of the run's instances are stored, with analysis plots broadly grouped as

- `evaluation`: plots of probes and times used as the evaluation dataset.
- `single_instance_plots`: outcomes of an individual QMLA instance, grouped by the instance ID. Includes results of training of individual models (in `model_training`), as well as sub-directories for analysis at the branch level (in `branches`) and comparisons.
- `combined_datasets`: pandas dataframes containing most of the data used during analysis of the run. Note that data on the individual model/instance level may be discarded so some minor analyses can not be performed offline.
- `exploration_strategy_plots` plots specifically required by the ES at the run level.
- `champion_models`: analysis of the models deemed champions by at least one instance in the run, e.g. average parameter estimation for a model which wins multiple instances.
- `performance`: evaluation of the QMLA run, e.g. the win rate of each model and the number of times each term is found in champion models.
- `meta analysis` of the algorithm's implementation, e.g. timing of jobs on each process in a cluster; generally users need not be concerned with these.

In order to produce the results presented in this thesis, the configurations listed in Table A.1 were input to the launch script. The launch scripts in the QMLA codebase consist of many configuration settings for running QMLA; only the lines in snippet in Listing A.1 need to be set according to altered to retrieve the corresponding figures. Note that the runtime of QMLA grows quite quickly with N_E, N_P (except for the `AnalyticalLikelihood` ES), especially for the entire QMLA algorithm; running QHL is feasible on a personal computer in < 30 minutes for $N_e = 1000; N_p = 3000$.

```
#!/bin/bash
```

```
#####
# QMLA run configuration
#####
num_instances=1
run_ghl=1 # perform QHL on known (true) model
run_ghl_muilt_model=0 # perform QHL for defined list of models.
exp=200 # number of experiments
prt=1000 # number of particles

#####
# QMLA settings
#####
plot_level=6
debug_mode=0

#####
# Choose an exploration strategy
#####

exploration_strategy='AnalyticalLikelihood'
```

Listing A.1: "QMLA Launch script"

Figure	Exploration Strategy	Algorithm	N_E	N_P	Data
??	AnalyticalLikelihood	QHL	500	2000	Nov_16/14_28
??	DemoIsing	QHL	500	5000	Nov_18/13_56
??	DemoIsing	QHL	1000	5000	Nov_18/13_56
??	DemoIsing	QHL	1000	5000	Nov_18/13_56
??	IsingLatticeSet	QMLA	1000	4000	Nov_19/12_04
	IsingLatticeSet	QMLA	1000	4000	Sep_30/22_40
??	HeisenbergLatticeSet	QMLA	1000	4000	Oct_22/20_45
	FermiHubbardLatticeSet	QMLA	1000	4000	Oct_02/00_09
	DemoBayesFactorsByFscore	QMLA	500	2500	Dec_09/12_29
??	DemoFractionalResourcesBayesFactorsByFscore	QMLA	500	2500	Dec_09/12_29
	DemoBayesFactorsByFscore	QMLA	1000	5000	Dec_09/12_29
	DemoBayesFactorsByFscoreEloGraphs	QMLA	500	2500	Dec_09/12_29

Table A.1: Implementation details for figures used in the main text.

EXAMPLE EXPLORATION STRATEGY RUN

A complete example of how to run the ;sqlmla framework, including how to implement a custom ES, and generate/interpret analysis, is given.

BIBLIOGRAPHY

- [1] Marcus W Doherty, Neil B Manson, Paul Delaney, Fedor Jelezko, Jörg Wrachtrup, and Lloyd CL Hollenberg. The nitrogen-vacancy colour centre in diamond. *Physics Reports*, 528(1):1–45, 2013.
- [2] Gordon Davies and MF Hamer. Optical studies of the 1.945 ev vibronic band in diamond. *Proceedings of the Royal Society of London. A. Mathematical and Physical Sciences*, 348(1653):285–298, 1976.
- [3] J Meijer, B Burchard, M Domhan, C Wittmann, Torsten Gaebel, I Popa, F Jelezko, and J Wrachtrup. Generation of single color centers by focused nitrogen implantation. *Applied Physics Letters*, 87(26):261909, 2005.
- [4] AM Edmonds, UFS D’Haenens-Johansson, RJ Cruddace, ME Newton, K-MC Fu, C Santori, RG Beausoleil, DJ Twitchen, and ML Markham. Production of oriented nitrogen-vacancy color centers in synthetic diamond. *Physical Review B*, 86(3):035201, 2012.
- [5] A Lenef and SC Rand. Electronic structure of the n-v center in diamond: Theory. *Physical Review B*, 53(20):13441, 1996.
- [6] Benjamin Smeltzer, Lilian Childress, and Adam Gali. ^{13}C hyperfine interactions in the nitrogen-vacancy centre in diamond. *New Journal of Physics*, 13(2):025021, 2011.
- [7] Heinz-Peter Breuer, Francesco Petruccione, et al. *The theory of open quantum systems*. Oxford University Press on Demand, 2002.
- [8] Antonio A. Gentile, Brian Flynn, Sebastian Knauer, Nathan Wiebe, Stefano Paesani, Christopher E. Granade, John G. Rarity, Raffaele Santagati, and Anthony Laing. Learning models of quantum systems from experiments, 2020.
- [9] MS Blok, Cristian Bonato, ML Markham, DJ Twitchen, VV Dobrovitski, and R Hanson. Manipulating a qubit through the backaction of sequential partial measurements and real-time feedback. *Nature Physics*, 10(3):189–193, 2014.
- [10] L Childress, MV Gurudev Dutt, JM Taylor, AS Zibrov, F Jelezko, J Wrachtrup, PR Hemmer, and MD Lukin. Coherent dynamics of coupled electron and nuclear spin qubits in diamond. *Science*, 314(5797):281–285, 2006.
- [11] Forrest T Charnock and TA Kennedy. Combined optical and microwave approach for performing quantum spin operations on the nitrogen-vacancy center in diamond. *Physical Review B*, 64(4):041201, 2001.

- [12] Antonio Andreas Gentile. *Operating practical quantum devices in the pre-threshold regime*. PhD thesis, University of Bristol, 2020.